

VALANCE BAND MAXIMUM AND THERMOELECTRIC PROPERTIES OF $\text{Bi}_2\text{O}_2\text{Se}$: FIRST-PRINCIPLES CALCULATIONS

TRAN VAN QUANG^{1,2,†}

¹*Department of Physics, University of Transport and Communications, Hanoi, Vietnam*

²*Duy Tan University, K7/25 Quang Trung, Hai Chau, Da Nang, Vietnam*

[†]*E-mail: tkuangv@gmail.com*

Received 5 April 2020

Accepted for publication 8 June 2020

Published 18 July 2020

Abstract. *Bismuth dioxide selenide, $\text{Bi}_2\text{O}_2\text{Se}$, is a thermoelectric material that exhibits low thermal conductivity. Detailed understanding of the compounds band structure is important in order to realize the potential of this narrow band semiconductor. The electronic band structure of $\text{Bi}_2\text{O}_2\text{Se}$ is examined using first - principles density functional theory and a primitive unit cell. The compound is found to be a narrow band gap semiconductor with very flat bands at the valence band maximum (VBM). VBM locates at points off symmetry lines. The energy surface at VBM is very flat. Nevertheless, these heavy bands do not reduce drastically the thermoelectric power factor. It is demonstrated by utilizing the solution of Boltzmann transport equation to compute the transport coefficients, i.e. the Seebeck coefficient, the electrical conductivity thereby the power factor and the electronic thermal conductivity. The electronic thermal conductivity and figure of merit of the compound are also estimated and discussed. The p-type doping is suggested for increasing the thermoelectric performance of the compound. All results are in good agreement with experiments and calculations reported earlier.*

Keywords: $\text{Bi}_2\text{O}_2\text{Se}$, band structure, primitive cell, valence band maximum, energy surface, thermoelectric, and first-principles calculation.

Classification numbers: 31.15.A-, 71.15.Mb, 72.20.Pa, 84.60.Rb, 71.20.-b, 71.20.Ps, 71.20.Mq, 71.20.Nr, 72.20.-I, 72.80.Cw.

I. INTRODUCTION

Recently, bismuth dioxide selenide $\text{Bi}_2\text{O}_2\text{Se}$ has been drawn much attention in the last few years in both theoretical and experimental studies including bulk and thin film [1–6]. It has been emerged as a promising candidate for future high-speed and low-power electronic applications due to the scalable fabrication of highly performing devices and excellent air stability and high-mobility semiconducting behavior [1–4, 7]. The compound exhibits several characteristics (low thermal conductivity, high electrical conductivity, and high Seebeck coefficient) that would highlight its potential in a practical thermoelectric (TE) application. The electronic band structure determines the transport properties [3, 8–10], so even though the compound was initially described as being a n-type semiconductor, p-type doping is theoretically possible [2, 11, 12]. More studies are needed especially on band topology at the valence band maximum (VBM). This determines the transport of hole carriers and the TE property of the compound.

To qualify the TE performance of a material or a device, one defines the dimensionless TE figure of merit [13], $ZT = \sigma^2 T / (\kappa_e + \kappa_L)$, where T is the temperature, S is the Seebeck coefficient, σ is the electrical conductivity, and κ_e and κ_L are the electronic and lattice thermal conductivity, respectively. Accordingly, a high ZT value is compulsory for the practical application, but the task is made challenging due to the fact that the increase of σ accompanies a decrease in S and an increase in κ_e and vice versa limits ZT . Physics behind this property stems from the interrelation between σ , S , κ_e and κ_L . Many methods have been used to improve the ZT of $\text{Bi}_2\text{O}_2\text{Se}$ including: making point defects [6, 11], introducing strains [14], nanostructure, etc. [15]. These methods do not improve the value of ZT to any considerable extent [15, 16]. The highest values of ZT for bulk materials are usually around unity or a little higher [13, 17–19]. The transport distribution function [20] is dependent on the electronic structure of materials, and defines the relationship between σ , S , and κ_e . These variables have the most adverse effect on ZT . The electronic structure allows us to explore many basic properties [8, 21], and plays a fundamental role in understanding materials. Detailed analysis of band structures at the valence band edge (especially the heavy band at the VBM) which determine the transport properties [3, 7, 22, 23], are still lacking. The use of a conventional unit cell for the calculation may lead to the folding of the energy bands which may obscure important information. These bands will have to be unfolded [24] in order to achieve a proper analysis. To circumvent the folded band a (real) triclinic primitive cell is used to carefully examine the band structure by employing first-principles density-functional-theory calculations. The thermoelectric coefficients are calculated as functions of temperature and doping level (in terms of energy dependence). Discussions are then made about improving the ZT of the compound.

II. COMPUTATIONAL DETAILS

As a typical bismuth-based oxychalcogenide material [25], the crystal structure of $\text{Bi}_2\text{O}_2\text{Se}$ is tetragonal. It consists of planar covalently bonded oxide layers (Bi_2O_2) sandwiched by Se square arrays with relatively weak electrostatic interaction [2, 12]. The primitive unit cell in Fig. 1(a) is used instead of the conventional tetragonal cell in Fig. 1(b). The most stable triclinic structure is obtained by seeking the lowest energy of the configuration via varied cell and ion dynamics relaxation. To perform calculation, first-principles density functional theory calculation [26, 27] has been addressed by using the generalized gradient approximation under PBE

method [28] as implemented in Quantum Espresso package [29, 30]. The convergence parameters of kinetic-energy cutoff E_{cut} (in Ry) for plane wave and Monkhorst-Pack k -point sampling grid [31, 32] have been carried out and checked. Accordingly, kinetic-energy cutoff of 64 Ry and k -point sampling grid of $7 \times 7 \times 7$ lead to the relevant convergence and have been used for further calculations. For the calculation of transport coefficients, the dense k -point grid of $23 \times 23 \times 23$ has been used.

To compute the transport coefficients, the solution of the Boltzmann transport equation in the constant relaxation-time approximation has been invoked. Hence, the electrical conductivity, the Seebeck coefficient, and the electronic thermal conductivity are determined by [20, 21, 33, 34]

$$\boldsymbol{\sigma} = \mathbf{I}^{(0)}, \quad (1)$$

$$\mathbf{S} = -\frac{1}{eT} \left(\mathbf{I}^{(0)} \right)^{-1} \mathbf{I}^{(1)}, \quad (2)$$

$$\kappa_e = \frac{1}{e^2 T} \left(\mathbf{I}^{(2)} - \mathbf{I}^{(1)} \mathbf{I}^{(0)^{-1}} \mathbf{I}^{(1)} \right). \quad (3)$$

where

$$\mathbf{I}^{(\alpha)} = e^2 \tau \int \frac{d\varepsilon d\mathbf{k}}{(2\pi)^3} \left(-\frac{\partial f}{\partial \varepsilon} \right) (\varepsilon - \mu)^\alpha \delta(\varepsilon - \varepsilon(\mathbf{k})) \mathbf{v}(\mathbf{k}) \mathbf{v}(\mathbf{k}), \quad (4)$$

in which τ , f , \mathbf{v} , δ are the relaxation time, the Fermi-Dirac distribution function, the group velocity, and the Dirac delta function, respectively; e is the elementary charge, μ is the chemical potential, and T is temperature. Different carrier concentrations were treated by the rigid band model [16]. The TE power factor is defined by $S^2 \sigma$. All the calculations are performed by using the BoltzTrap code [33, 34].

III. RESULTS AND DISCUSSIONS

To determine the crystal-structure, the cell shape and volume were varied. The relaxation was performed using the triclinic primitive unit cell. It is found that the most stable structure corresponds to the crystal structure with lattice constants $a = b = c = 6.84 \text{ \AA}$ and $\alpha = \beta = 146.45^\circ$, $\gamma = 48.18^\circ$. The structure is depicted in Fig. 1 (a) for the primitive cell together with the tetragonal conventional cell in Fig. 1 (b) for a comparison. The first Brillouin zone (BZ) corresponding to the primitive cell is illustrated in Fig. 1(c) [35]. To elaborate the band structure carefully, we compute energy bands along the high symmetry lines from Z to Γ , i.e. X - Γ - Y - Y1 - Y2 - Y3 - Y4 - Y5 - Y6 - L - Γ - Z - Z1 - Z2 - Z3 - N - Γ - M - M1 - M2 - M3 - Γ - R - Y1 - R1 - Γ (Their coordinates are given in the Appendix). The calculated band structure is presented in Fig. 2. It is found that $\text{Bi}_2\text{O}_2\text{Se}$ is a narrow band gap semiconductor with the band gap of about 0.29 eV. It is smaller compared to the experimental band gap of $\sim 0.8 \text{ eV}$ [1, 36] and to our precise-full potential calculated band gap of $\sim 0.78 \text{ eV}$ [2]. This originates from the underestimation of calculated band gaps within LDA and GGA calculations [2, 37]. We pointed out in Ref. [2] that the band topology of $\text{Bi}_2\text{O}_2\text{Se}$, especially the band edges (near Fermi energy), including the position of valence band maximum (VBM) and conduction band minimum (CBM), does not alter by using different approaches, i.e. LDA, LDA+SOC, sX-LDA, and sX-LDA-SOC (see Ref. [2]).

As can be seen, CBM occurs at Γ which is in good agreement with calculations reported previously [2, 3, 38]. The second-lowest points at the conduction band edges are at the L and M points. These two points can be considered as one point in the first irreducible BZ (see Fig. 1(c)).

These bands, including the CBM band, are relatively largely dispersive which indicates the light carrier mass leading to the high mobility. These features are responsible for high σ reported below.

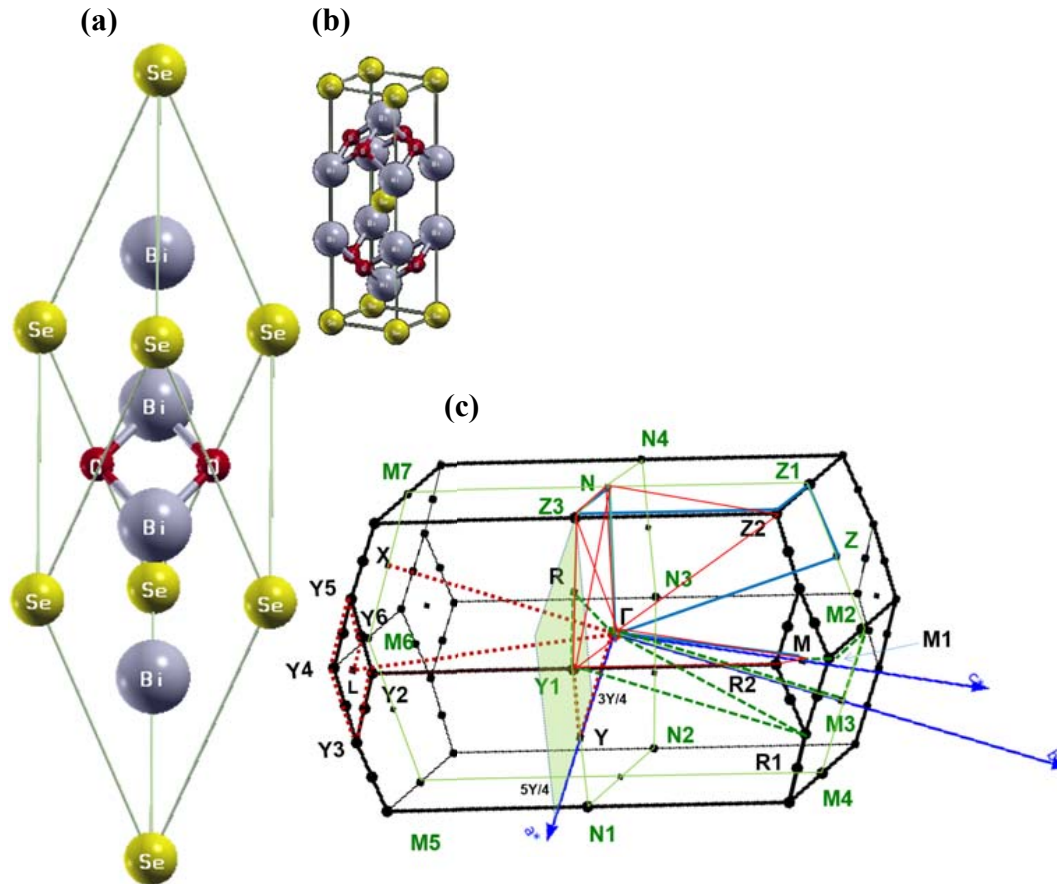


Fig. 1. (a) Primitive, (b) conventional unit cells and (c) the first Brillouin zone with special k-points of $\text{Bi}_2\text{O}_2\text{Se}$.

To take a close look and highlight VBM, we select the path $N - Z3 - Y1 - N1 - N2 - N3 - N4 - N - \Gamma - M3 - M4 - M5 - M6 - M7 - Z1 - M2 - M3$ and perform the calculation. The results are presented in Fig. 3. As can be seen, VBM occurs along the lines $Z3 - N1$, $N2 - N4$, $M3 - M4$, $M5 - M7$, $Z1 - M3$. The band is very flat and separated from others. This is attributed to the strong direction dependence of VBM which relates to the dispersive band at $Z3$ ($Z2 - Z3 - N$ direction). We also verify this feature by doing a band calculation in the $(\Gamma YY1)$ plane to show the energy surface for the valence band edge. The result is presented in Fig. 4. As can be shown, the VBM is off symmetry point. Heavy bands at VBM develop sharply the density of states (DOS) as shown in Fig. 5, which is responsible for the enhancement of the Seebeck coefficient. Instantaneously, it is detrimental for the mobility of charge carriers as well. However, this detrimental effect can be reduced due to two reasons: the dispersive SHVBM

increasing the mobility and the directional dependence of the energy surface, leading to relative high directional average of the mobility.

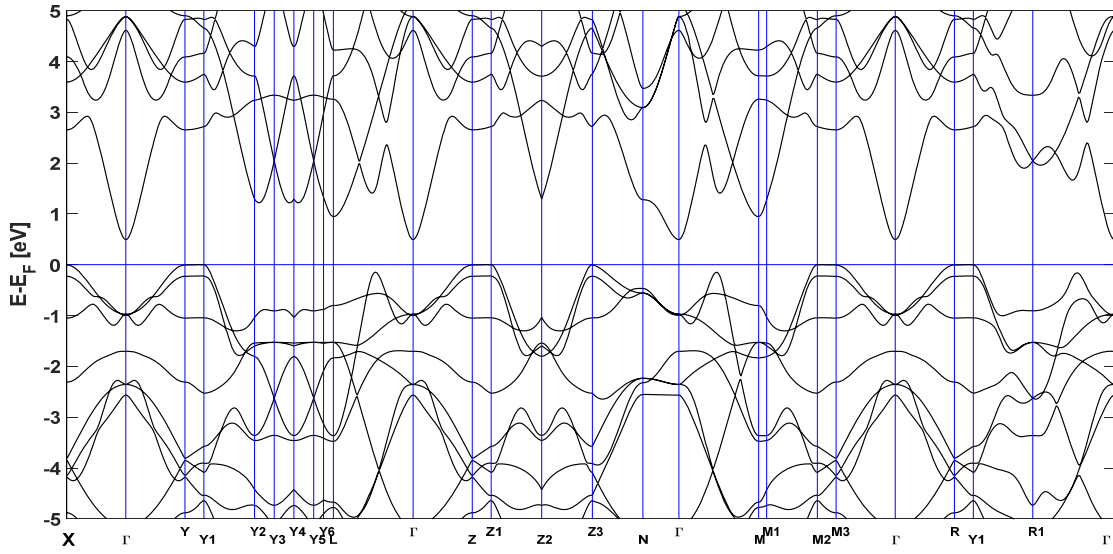


Fig. 2. Calculated band structure of $\text{Bi}_2\text{O}_2\text{Se}$ using primitive cell.

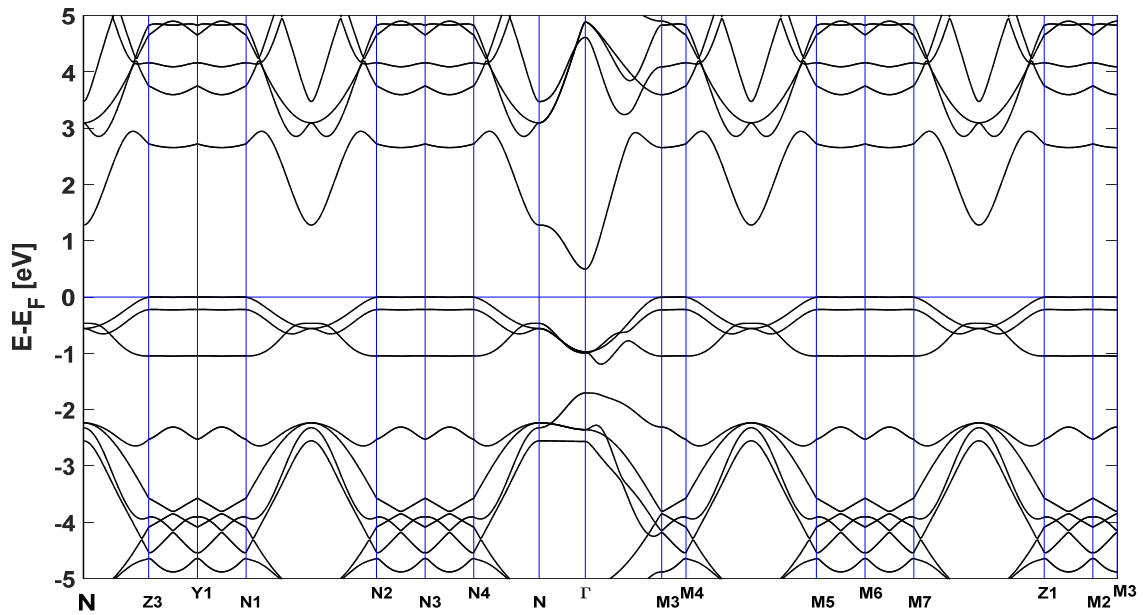


Fig. 3. Calculated band structure of $\text{Bi}_2\text{O}_2\text{Se}$ using primitive cell along the conduction band minimum and valence band maximum lines.

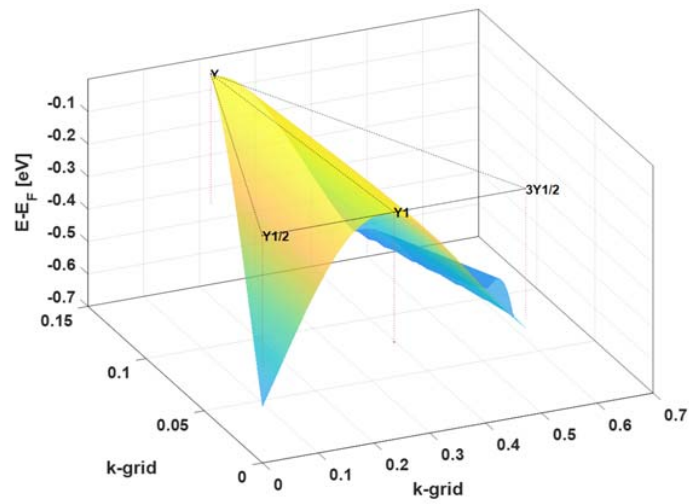


Fig. 4. Fermi surface around the valence band edge.

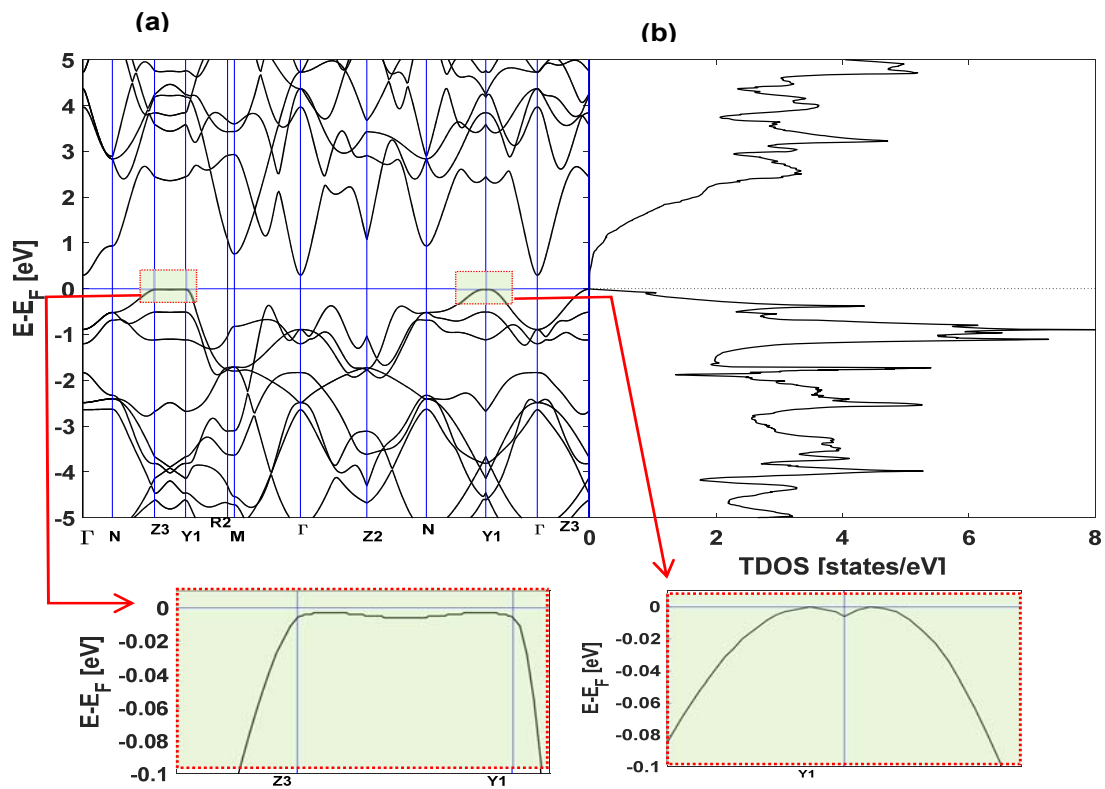


Fig. 5. (a) Calculated band structure along selected paths (see Fig. 1(c)) and (b) density of states of $\text{Bi}_2\text{O}_2\text{Se}$.

The valence bands are more complicated. The valence band maximum (VBM) occurs along YY1, ZZ1, M2M3, RY1, and at Z3 with less dispersive band, except at Z3 whereas the second-highest valence band maximum (SHVBM) occurs at a point along Γ L, Γ M and Γ R1 with relative small curvature, i.e. more dispersive.

The surface shows exactly what we expected, i.e. the band is dispersive in the Γ Y1 direction and flat in the YY1 direction. Accordingly, the mobility is high along the Γ Y1 direction and low along the YY1 direction. Therefore, the average of the electrical conductivity thereby the power factor is not low. This point will be demonstrated by performing calculation of the power factor below. Together with the results above (Fig. 2), we can see the tetragonal symmetry of the bands. The bands thereby can be examined using $\Gamma - N - Z3 - Y1 - R2 - M - \Gamma - Z2 - N - Y1 - \Gamma - Z3$ path which is indicated by red lines in Fig. 1(c). To examine we continue to calculate the energy bands along this path and the total DOS. The results are displayed in Fig. 6(a) for band structure with VBM zooming up and (b) DOS. As can be seen, VBM is off symmetry. And the slope of DOS at the valence band edge is very steep. This stems from the flat bands as presented above. This is in good agreement with previous publications in which DOS at valence band edge is very sharp [2, 39, 40]. The dispersive bands occurring at SHVBM are also interesting and these also contribute partially to the transport properties of $\text{Bi}_2\text{O}_2\text{Se}$.

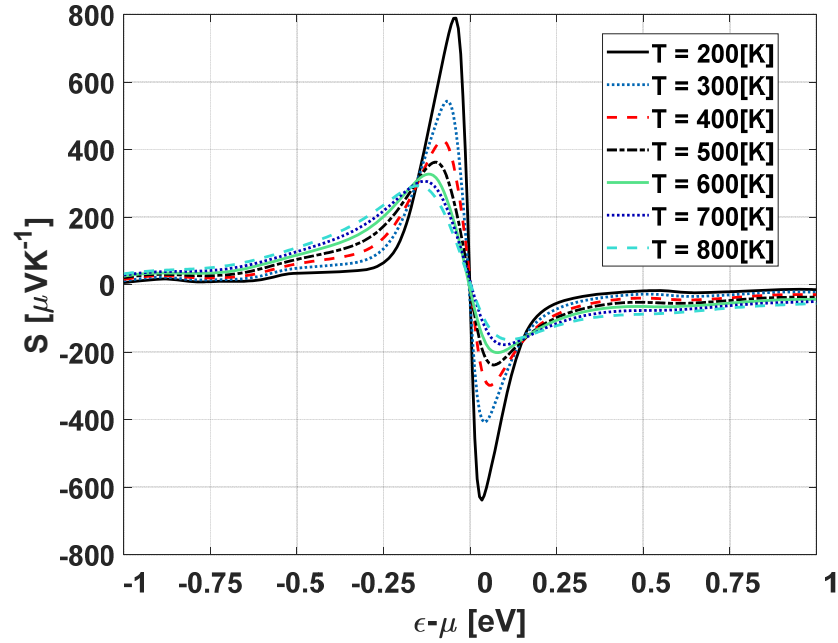


Fig. 6. (Color online) Seebeck coefficient, S (in $\mu\text{V}/\text{K}$), as functions of concentration chemical potential $\varepsilon - \mu$ with various temperatures.

To demonstrate, we compute the transport coefficients, i.e. the Seebeck coefficient S , the electrical conductivity σ , the electronic thermal conductivity κ_e , the power factor, and estimate the figure of merit ZT_e as a function of energy level referred to the chemical potential μ at various temperatures, i.e. $T = 200, 300, 400, 500, 600, 700,$ and 800K . The result of S is displayed

in Fig. 6. As can be seen, at small doping levels, the Seebeck coefficient is reduced with the increase in temperature. This stems from the bipolar conduction effect in which the intrinsic carriers get across the bandgap by thermal excitation lowering the Seebeck coefficient. The large maximum achieved at a relevant optimal doping level indicates $\text{Bi}_2\text{O}_2\text{Se}$ to be a good thermoelectric material. At doping level of 0.22 eV, at room temperature, S is $-113 \mu\text{V/K}$ meanwhile the experiment reported S of $-118 \mu\text{V/K}$ at 300 K. This is consistent with other calculations and experiments [2, 6, 11, 12]. At the same temperature, for the p-type doping is greater than that for n-type doping. It originates from the large steep DOS at the valence band edge as proved in the band structure calculation above [20].

However, the heavy bands (at VBM) are usually leading to low σ due to the fact that it determines the heavy mass of carriers (holes) thereby the low mobility. If it is the case, the power factor, $S^2\sigma$, is decreased. However, our calculated results show that the power factor is still relatively large. To show, we calculated the power factor as the function of energy at various temperatures. The results are shown in Fig. 7 and Fig. 8. The power factor for p-type doping is significantly greater than that for n-type doping, especially the maximum value at the appropriate optimal doping level as shown in Fig. 8. As can be seen, if the relaxation time is about 10^{-14}s [2, 9, 41], then the maximum power factors at room temperature are about $7 \times 10^{-4} \text{Wm}^{-1}\text{K}^{-2}\text{s}^{-1}$ for n-type doping and $25 \times 10^{-4} \text{Wm}^{-1}\text{K}^{-2}\text{s}^{-1}$ for p-type doping which is similar to the maximum value of the well-known thermoelectric material, Bi_2Te_3 , with the value of about $30 \times 10^{-4} \text{Wm}^{-1}\text{K}^{-2}\text{s}^{-1}$ [42]. Moreover, the power factor is monotonically increased with temperature in both doping types. It is in good agreement with previous reports [2, 40].

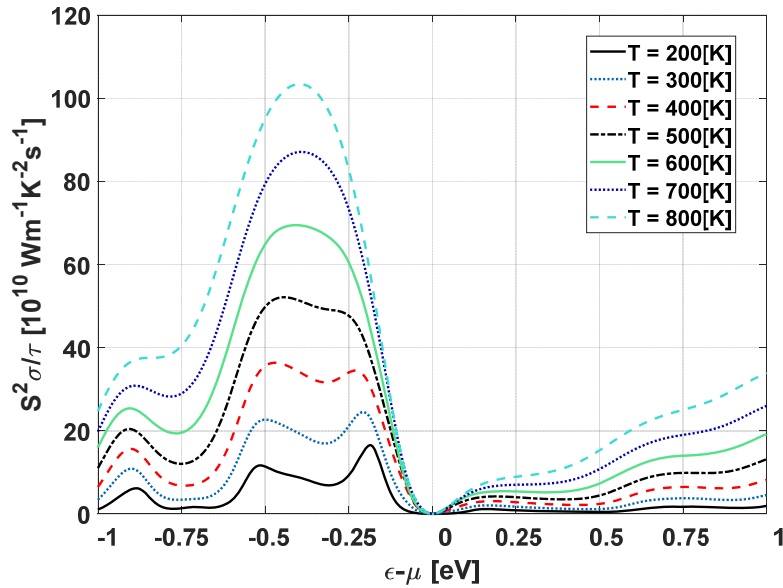


Fig. 7. (Color online) The relaxation-time-dependent power factor, $S^2\sigma/\tau$ (unit in $10^{10} \text{Wm}^{-1}\text{K}^{-2}\text{s}^{-1}$) as a function of chemical potential $\epsilon - \mu$ with various temperatures.

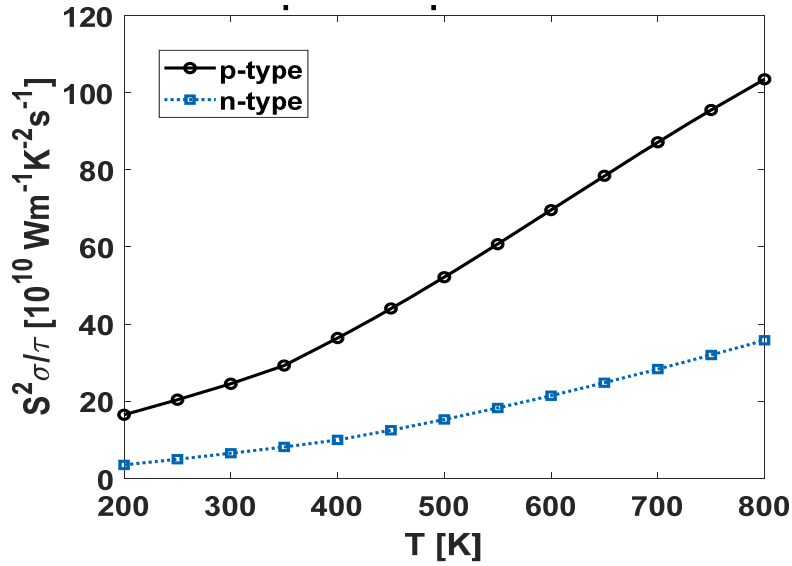


Fig. 8. (Color online) Maximum relaxation-time-dependent power factor, $S^2\sigma/\tau$ (unit in $10^{10} \text{ Wm}^{-1} \text{ K}^{-2} \text{ s}^{-1}$) as a function of temperature.

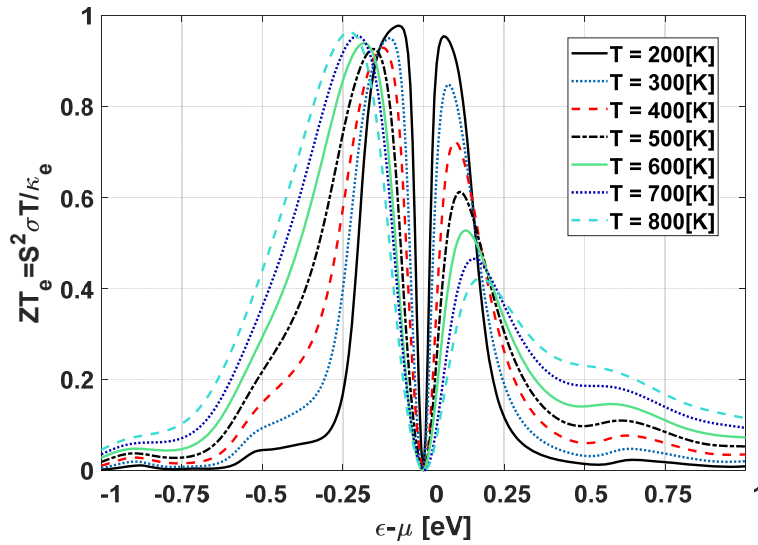


Fig. 9. (Color online) ZT_e , $S^2\sigma T/\kappa_e$ as a function of chemical potential $\epsilon - \mu$ with various temperatures.

To estimate the contribution of thermal conductivity to the thermoelectric performance, we calculate the electronic part κ_e , and compute $ZT_e = S^2\sigma T/\kappa_e$, which is the figure of merit ZT provided by the small lattice thermal conductivity as reported previously [12]. The calculated result is displayed in Fig. 9. Accordingly, ZT_e strongly depends on the doping level. With the

optimal doping levels, it may reach 0.9 ~ 1.0 for p-type doping whereas with the n-type doping, the maximum value is drastically reduced with temperature. This originates from the rapid increase of the electronic thermal conductivity with the increase in temperature. At doping level of $E = 0.18$ eV, ZT at 780 K is about 0.3 and with higher doping levels, ZT thereby ZT is monotonically increased with the increase of temperature. It is consistent with experiment [43] in which ZT is about 0.24 at 780 K and it is monotonically increased with temperature.

IV. CONCLUSIONS

By using the triclinic primitive cell, we performed first-principles density-functional-theory calculation to carefully study the band structure of Bi₂O₂Se. We find that Bi₂O₂Se is a narrow band gap semiconductor with the band gap of about 0.29 eV. The VBM is off symmetry lines leading to its high degeneracy. The curvature of the energy band at VBM is strongly directional dependent. It is flat along the boundary of BZ and dispersive along the perpendicular direction. Together with the contribution to the electrical conductivity from the dispersive SHVBM the electrical conductivity of p-type doping is not drastically reduced. As a result, the power factor is relatively high. The estimated ZT exhibits significant enhancement by optimizing the carrier concentration. The maximum ZT is almost unchanged in p-type doping and reduced in n-type doping with the increase of temperature whereas at an appropriate fixed higher doping level for n-type doping. ZT is increased with the increase of temperature. The calculated results are in good agreement with experiments and calculations reported previously.

REFERENCES

- [1] J. Wu, H. Yuan, M. Meng, C. Chen, Y. Sun, Z. Chen, W. Dang, C. Tan, Y. Liu, J. Yin, Y. Zhou, S. Huang, H.Q. Xu, Y. Cui, H.Y. Hwang, Z. Liu, Y. Chen, B. Yan, H. Peng, *Nat. Nanotechnol.* **12** (2017) 530.
- [2] T. Quang, H. Lim, M. Kim, *J. Korean Phys. Soc.* **61** (2012) 1728.
- [3] S. V. Eremeev, Y.M. Koroteev, E. V. Chulkov, *Phys. Rev. B* **100** (2019) 115417.
- [4] J. Liu, L. Tian, Y. Mou, W. Jia, L. Zhang, R. Liu, *J. Alloys Compd.* **764** (2018) 674.
- [5] J.H. Song, H. Jin, A.J. Freeman, *Phys. Rev. Lett.* **105** (2010) 096403.
- [6] T. Van Quang, M. Kim, *J. Appl. Phys.* **120** (2016) 195105.
- [7] H. Fu, J. Wu, H. Peng, B. Yan, *Phys. Rev. B* **97** (2018) 1.
- [8] T. Van Quang, K. Miyoung, *J. Korean Phys. Soc.* **74** (2019) 256.
- [9] T. Van Quang, M. Kim, *J. Appl. Phys.* **113** (2013) 17A934.
- [10] T. Van Quang, M. Kim, *IEEE Trans. Magn.* **50** (2014) 1000904.
- [11] P. Ruleova, T. Plechacek, J. Kasparova, M. Vlcek, L. Benes, P. Lostak, C. Drasar, *J. Electron. Mater.* **47** (2018) 1459.
- [12] P. Ruleova, C. Drasar, P. Lostak, C.P. Li, S. Ballikaya, C. Uher, *Mater. Chem. Phys.* **119** (2010) 299.
- [13] G.J. Snyder, E.S. Toberer, *Nat. Mater.* **7** (2008) 105–114.
- [14] D. Guo, C. Hu, Y. Xi, K. Zhang, *J. Phys. Chem. C* **117** (2013) 21597.
- [15] L. Pan, L. Zhao, X. Zhang, C. Chen, P. Yao, C. Jiang, X. Shen, Y. Lyu, C. Lu, L.D. Zhao, Y. Wang, *ACS Appl. Mater. Interfaces* **11** (2019) 21603.
- [16] M. Liangruksa, *Mater. Res. Express* **4** (2017) 035703.
- [17] X. Zhang, L.-D. Zhao, *J. Mater.* **1** (2015) 92.
- [18] K. Biswas, J. He, I.D. Blum, C.-I. Wu, T.P. Hogan, D.N. Seidman, V.P. Dravid, M.G. Kanatzidis, *Nature* **489** (2012) 414.
- [19] Y. Pei, H. Wang, G.J. Snyder, *Adv. Mater.* **24** (2012) 6125.
- [20] G.D. Mahan, J.O. Sofo, *Proc. Natl. Acad. Sci.* **93** (1996) 7436.
- [21] T. Van Quang, *Commun. Phys.* **28** (2018) 169.

- [22] T. Cheng, C. Tan, S. Zhang, T. Tu, H. Peng, Z. Liu, *J. Phys. Chem. C* **122** (2018) 19970.
- [23] Q.D. Gibson, M.S. Dyer, G.F.S. Whitehead, J. Alaria, M.J. Pitcher, H.J. Edwards, J.B. Claridge, M. Zanella, K. Dawson, T.D. Manning, V.R. Dhanak, M.J. Rosseinsky, *J. Am. Chem. Soc.* **139** (2017) 15568.
- [24] W. Ku, T. Berlijn, C.C. Lee, *Phys. Rev. Lett.* **104** (2010) 216401.
- [25] T. Van Quang, M. Kim, *J. Appl. Phys.* **122** (2017) 245104.
- [26] P. Hohenberg, W. Kohn, *Phys. Rev.* **136** (1964) B864.
- [27] W. Kohn, L.J. Sham, *Phys. Rev.* **140** (1965) A1134–A1138.
- [28] J.P. Perdew, K. Burke, M. Ernzerhof, *Phys. Rev. Lett.* **77** (1996) 3865.
- [29] P. Giannozzi, S. Baroni, N. Bonini, M. Calandra, R. Car, C. Cavazzoni, D. Ceresoli, G.L. Chiarotti, M. Cococcioni, I. Dabo, A.D. Corso, S. Fabris, G. Fratesi, S. de Gironcoli, R. Gebauer, U. Gerstmann, C. Gougoussis, A. Kokalj, M. Lazzeri, L. Martin-samos, N. Marzari, F. Mauri, R. Mazzarello, S. Paolini, A. Pasquarello, L. Paulatto, C. Sbraccia, S. Scandolo, G. Sclauzero, A.P. Seitsonen, A. Smogunov, P. Umari, R.M. Wentzcovitch, S. De Gironcoli, S. Fabris, G. Fratesi, R. Gebauer, U. Gerstmann, C. Gougoussis, A. Kokalj, M. Lazzeri, L. Martin-samos, N. Marzari, F. Mauri, R. Mazzarello, S. Paolini, A. Pasquarello, L. Paulatto, C. Sbraccia, A. Smogunov, P. Umari, *J. Phys. Condens. Matter* **21** (2009) 395502.
- [30] P. Giannozzi, O. Andreussi, T. Brumme, O. Bunau, M. Buongiorno Nardelli, M. Calandra, R. Car, C. Cavazzoni, D. Ceresoli, M. Cococcioni, N. Colonna, I. Carnimeo, A. Dal Corso, S. De Gironcoli, P. Delugas, R.A. Distasio, A. Ferretti, A. Floris, G. Fratesi, G. Fugallo, R. Gebauer, U. Gerstmann, F. Giustino, T. Gorni, J. Jia, M. Kawamura, H.Y. Ko, A. Kokalj, E. Küçükbenli, M. Lazzeri, M. Marsili, N. Marzari, F. Mauri, N.L. Nguyen, H. V. Nguyen, A. Otero-De-La-Roza, L. Paulatto, S. Poncé, D. Rocca, R. Sabatini, B. Santra, M. Schlipf, A.P. Seitsonen, A. Smogunov, I. Timrov, T. Thonhauser, P. Umari, N. Vast, X. Wu, S. Baroni, *J. Phys. Condens. Matter* **29** (2017) 465901.
- [31] H. Monkhorst, J. Pack, *Phys. Rev. B* **13** (1976) 5188.
- [32] J.D. Pack, H.J. Monkhorst, *Phys. Rev. B* **16** (1977) 1748.
- [33] G.K.H. Madsen, J. Carrete, M.J. Verstraete, *Comput. Phys. Commun.* **231** (2018) 140–145.
- [34] G.K.H. Madsen, D.J. Singh, *Comput. Phys. Commun.* **175** (2006) 67.
- [35] A. Kokalj, *J. Mol. Graph. Model.* **17** (1999) 176.
- [36] C. Chen, M. Wang, J. Wu, H. Fu, H. Yang, Z. Tian, T. Tu, H. Peng, Y. Sun, X. Xu, J. Jiang, N.B.M. Schröter, Y. Li, D. Pei, S. Liu, S.A. Ekahana, H. Yuan, J. Xue, G. Li, J. Jia, Z. Liu, B. Yan, H. Peng, Y. Chen, *Sci. Adv.* **4** (2018) 1.
- [37] A. Seidl, A. Görling, P. Vogl, J. Majewski, M. Levy, *Phys. Rev. B* **53** (1996) 3764.
- [38] L. Pan, W. Di Liu, J.Y. Zhang, X.L. Shi, H. Gao, Q. feng Liu, X. Shen, C. Lu, Y.F. Wang, Z.G. Chen, *Nano Energy* **69** (2020) 104394.
- [39] N. Wang, M. Li, H. Xiao, H. Gong, Z. Liu, X. Zu, L. Qiao, *Phys. Chem. Chem. Phys.* **21** (2019) 15097.
- [40] D. Guo, C. Hu, Y. Xi, K. Zhang, *J. Phys. Chem. C* **117** (2013) 21597–21602.
- [41] T. Van Quang, K. Miyoung, *J. Korean Phys. Soc.* **68** (2016) 393–397.
- [42] M.S. Park, J.H. Song, J.E. Medvedeva, M. Kim, I.G. Kim, A.J. Freeman, *Phys. Rev. B* **81** (2010) 155211.
- [43] A. L. J. Pereira, D. Santamaría-Pérez, J. Ruiz-Fuertes, F.J. Manjón, V.P. Cuenca-Gotor, R. Vilaplana, O. Gomis, C. Popescu, A. Munoz, P. Rodríguez-Hernández, A. Segura, L. Gracia, A. Beltrán, P. Ruleova, C. Drasar, J.A. Sans, *J. Phys. Chem. C* **122** (2018) 8853.

APPENDIX

The choice of symmetry points in BZ is given here (see Table 1). The coordinates of symmetry k-points are given in fractions of the primitive reciprocal vectors \mathbf{a}^* , \mathbf{b}^* , and \mathbf{c}^* (see Fig. 1(c)).

Table 1. Coordinates of symmetry k-points of the primitive cell $\text{Bi}_2\text{O}_2\text{Se}$ lattice.

Point	\mathbf{a}^*	\mathbf{b}^*	\mathbf{c}^*
Γ	0.00000	0.00000	0.00000
L	0.50000	-0.50000	0.00000
M	0.00000	0.00000	0.50000
M1	-0.05089	0.05089	0.50000
M2	-0.27544	0.27545	0.27545
M3	0.00000	0.50000	0.00000
M4	0.27551	0.72449	-0.27551
M5	0.72449	0.27551	-0.72449
M6	0.27551	-0.27551	-0.27551
M7	-0.27551	-0.72449	0.27551
N	-0.50000	-0.50000	0.50000
N1	0.72449	0.27551	-0.27551
N2	0.27551	0.72449	-0.72449
N3	-0.27551	0.27551	-0.27551
N4	-0.72449	-0.27551	0.27551
R	0.00000	-0.50000	0.50000
R1	0.24993	0.24993	0.25007
R2	0.05089	-0.05089	0.50000
X	0.00000	-0.50000	0.00000
Y	0.50000	0.00000	0.00000
Y1	0.27545	-0.27544	0.27545
Y2	0.50001	-0.49999	0.05090
Y3	0.75007	-0.24993	-0.25007
Y4	0.49999	-0.50001	-0.05090
Y5	0.24993	-0.75007	0.25007
Y6	0.37497	-0.62503	0.15049
Z	-0.50000	0.00000	0.50000
Z1	-0.72449	-0.27551	0.72449
Z2	-0.50001	-0.50001	0.94910
Z3	-0.27551	-0.72449	0.72449